PERGAMON

Acta mater. Vol. 47, No. 8, pp. 2345–2356, 1999

PII: S1359-6454(99)00115-9
1359-6454/99 $20.00 + 0.00

EVOLUTION OF THE SIDEBRANCH STRUCTURE IN FREE DENDRITIC GROWTH

Q. LI and C. BECKERMANN†

Department of Mechanical Engineering, The University of Iowa, Iowa City, IA 52242, U.S.A.

(Received 14 January 1999; accepted 14 April 1999)

Abstract—The sidebranching behavior in free dendritic growth into a supercooled melt is investigated through a detailed measurement of the sidebranch structure of succinonitrile (SCN) dendrites using images from the microgravity experiment of Glicksman and co-workers. The measurements show that the sidebranching evolution is divided into two regimes: an initial linear regime and a subsequent non-linear coarsening regime. A simple model, based on the Mullins–Sekerka linear stability theory, is developed to describe the initial sidebranching behavior. The excellent agreement of the model prediction with the experimental results indicates that the initial sidebranch spacings are selected by the maximum instability wavelength. In the non-linear regime, two new geometrical parameters, derived from the measurements, are proposed to characterize the coarsening process of the sidebranches and to compare the measurements with available coarsening theories. It is found that coarsening at the sidebranch roots follows closely classical laws for purely capillary-driven isothermal coarsening, but the overall coarsening process of the entire sidebranching dendrite cannot be explained by these isothermal coarsening theories. © *1999 Acta Metallurgica Inc. Published by Elsevier Science Ltd. All rights reserved.*

Keywords: Dendritic growth; Phase transformations; Dynamic phenomena; Interface; Microstructure

1. INTRODUCTION

The sidebranching phenomenon in dendritic growth has recently received increased research attention. To metallurgical engineers sidebranches are important because they establish the length scales and pattern of microsegregation, and therefore determine the properties of solidified materials. Due to its rich behavior as a non-linear phase transformation process, the sidebranching phenomenon is also of interest to physicists. Here, we focus on sidebranching in free dendritic growth into an essentially infinite volume of an initially uniformly supercooled melt of a pure substance. A typical freely grown dendrite branch is shown in Fig. 1.

The formation of dendritic sidebranches can generally be attributed to the Mullins–Sekerka instability [1]. Based on this idea, Langer and Müller-Krumbhaar developed the marginal stability theory [2] that ascribes the sidebranching to an intrinsic morphological instability of the needle crystal — with the tip persisting in a marginal state of interfacial stability. Later, Langer and coworkers [3–5] investigated the thermal noise amplification mechanism for sidebranching, which has become the preferred explanation for the sidebranching phenomenon. In particular, Langer's three-dimensional symmetric approach [4], based on a paraboloidal needle crystal, predicts that the amplitude of the perturbations grows with the distance Z from the dendrite tip exponentially as a function of $(Z^{1/4}/\sigma^{1/2})$ and the characteristic wavelength, λ, in units of the tip radius R, is given by

$$\lambda/R = 2^{1/4}\pi\sqrt{6\sigma}(Z/R)^{1/4} \approx 1.29(Z/R)^{1/4} \quad (1)$$

where σ is the usual selection constant [$\approx$0.02 for succinonitrile (SCN)]. However, a comparison between this model and the experimental results of Huang and Glicksman [6] shows only approximate, qualitative agreement and the experimentally observed sidebranches have much larger amplitudes than can be explained by purely thermal noise in the model.

Brener and Temkin [7] have studied the time-dependent behavior of sidebranch formation taking into account the nonaxisymmetric, three-dimensional needle crystal shape as proposed by Brener [8]. This model predicts much faster-growing sidebranch amplitudes than Langer's symmetric model and the characteristic wavelength is given by

$$\lambda/R = 2\pi(3/5)^{3/10}\sqrt{3\sigma}(Z/R)^{1/5} \approx 1.32(Z/R)^{1/5}. \quad (2)$$

The predicted sidebranch amplitudes are found to be in reasonable agreement with the experiment of Bisang and Bilgram [9, 10] for xenon dendrites and with the experiment of LaCombe *et al.* [11] for SCN dendrites [10]. These studies confirm that the sidebranches are indeed triggered by thermal noise. However, it is shown below that available measurements of the initial sidebranch spacing are only approximately predicted by either equation (1) or equation (2).

†To whom all correspondence should be addressed.

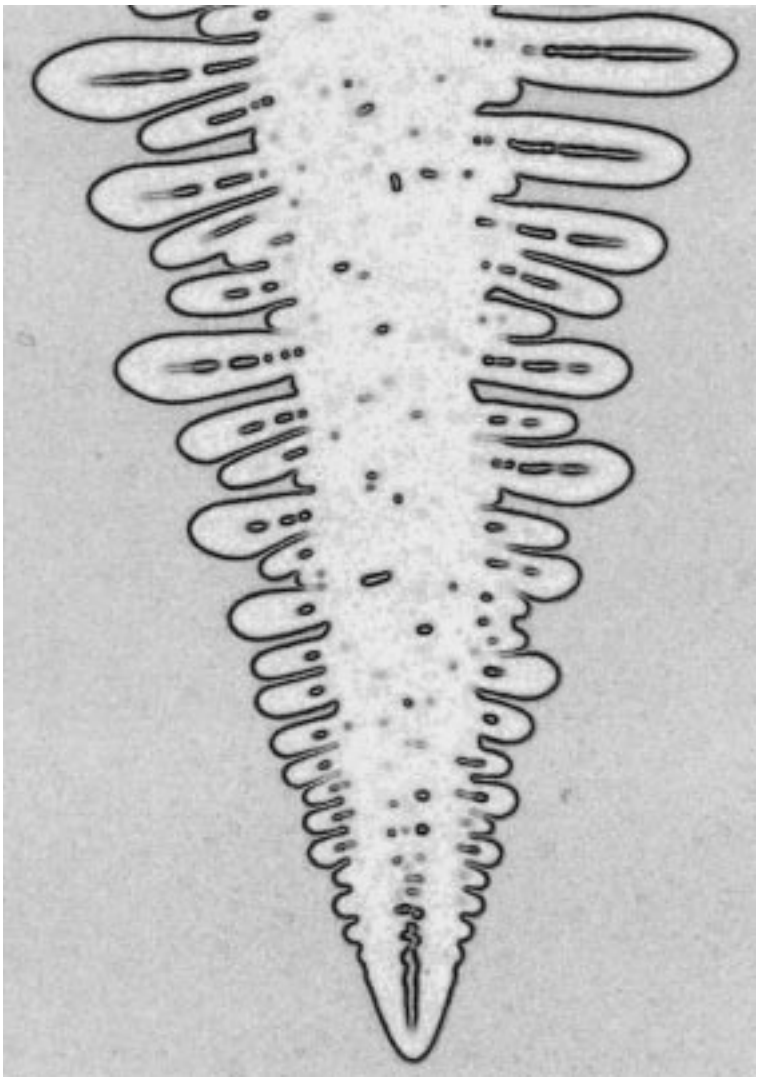

Fig. 1. Example of a sidebranching dendrite growing into a supercooled melt; the image is from the microgravity experiment of Glicksman *et al.* [15] for SCN.

The above-mentioned models only deal with the initial, linear sidebranching behavior — a relatively narrow regime near the tip. As is apparent from Fig. 1, further away from the tip the sidebranches lose their periodicity. Longer sidebranches continue to grow into the supercooled melt, while shorter ones dissolve or grow together and the primary stem thickens. Experiments by Hürlimann *et al.* [12] using xenon and Dougherty and Chen [13] using a NH_4Cl solution, as well as the measurements of Li and Beckermann [14] on SCN dendrites, have demonstrated that the sidebranch structure far from the tip is still self-similar and geometrical parameters, such as the contour length and projection area, can be scaled with the tip radius R. Brener and Temkin [7] have shown that this strongly nonlinear growth regime is self-similar up to $Z/R \ll 1/Pe$, where Pe is the tip Peclet number. For the relatively low supercoolings present in many dendritic growth experiments, the self-similar regime can thus be several hundred tip radii long. Brener and Temkin's scaling analysis indicates that competitive growth between sidebranches leads to the spacing between the active, longer sidebranches increasing linearly with distance from the primary dendrite tip. The inactive, shorter sidebranches evolve in an essentially isothermal environment between the active branches [6]. Their spacing and diameter also increase as a function of distance from the tip or time in a process that may be associated with classical isothermal coarsening driven by a reduction in the surface free energy (or curvature). Because the sidebranch spacing and diameter are difficult to define in the non-linear regime, Hürlimann *et al.* [12] and Li and Beckermann [14] have measured the contour length, U, and the projection area, F, in the sidebranch plane of the dendrite as a function of the distance from the tip. These measurements include both the growing and shrinking sidebranches. Both studies find that the

projection area increases linearly with the contour length and that the slope of $F(U)$ normalized with the tip radius R is a constant independent of the supercooling. In other words, the ratio U/F, which can be interpreted as an interfacial length concentration, does not vary with distance from the tip or time in the self-similar regime $1 \ll Z/R \ll 1/Pe$. This astonishing linear behavior has not been explained theoretically, although Hürlimann *et al.* [12] have proposed a simple rod model. The fact that the normalized interfacial length concentration is a constant would suggest that coarsening is absent in the non-linear regime. More likely, an increase in the interfacial length concentration due to sidebranch growth into the supercooled melt may be "canceled" by a decrease due to isothermal coarsening. While the competitive growth of the active sidebranches is well explained by Brener and Temkin's theory [7], the role of capillary-driven coarsening and the spacing adjustment mechanisms for all sidebranches in free dendritic growth are apparently in need of further investigation.

In this paper we continue our measurements [14] of single SCN dendrites growing freely into a supercooled melt, using images from the microgravity experiments of Glicksman *et al.* [15], and investigate the evolution of the secondary dendrite arm spacing and the coarsening of the sidearm structure. The measurements clearly identify the linear and non-linear sidebranching regimes mentioned above. A simple model is developed to explain the behavior of the initial nearly periodic sidebranches. The model is then compared with the previous theories [equations (1) and (2)] and our spacing measurements. In the subsequent non-linear sidebranching regime, none of the existing geometrical parameters are found to be appropriate for comparison with classical coarsening theories. We therefore propose two new parameters in order to understand the coarsening mechanisms of the dendritic sidebranches. One is the root radius, ρ_r, which is obtained from the measured arm spacings and represents the (inverse) curvature in the region near the sidebranch roots. The other is a mean sidebranch radius, ρ_m, that is intended to characterize the average curvature of an entire sidebranch. Both radii are compared to available coarsening theories.

2. MEASUREMENT PROCEDURES

The primary source of three-dimensional dendrite information used in this investigation are photographs, in the form of orthogonal pairs of digitized binary images, from the microgravity experiment of Glicksman *et al.* [15] for free dendritic growth of SCN into a uniformly supercooled melt (see Fig. 1 as an example). We use the same analysis technique as in our previous work [14] to process these images. After some steps, we obtain two-dimensional reconstructions of the dendrite images oriented in the sidebranch plane (see Fig. 2). Our measurements of sidebranching dendrites are performed on these reconstructed images.

The critical measurement in this investigation is the secondary arm spacing, λ, which is the most frequently used, and perhaps most important, parameter to describe the evolution and structure of sidebranching dendrites. Unfortunately, it is not a well-defined parameter due to the very irregular nature of the sidebranch structure, particularly in the non-linear regime. Two extreme methods can be considered in measuring the spacing. One is to count every existing branch, no matter whether it is growing or shrinking. Another extreme is to count only the actively growing branches which form the envelope of the dendrite. In the latter method, the spacing adjustment is controlled only by the competitive branch growth mechanism discussed by Brener and Temkin [7]. Since we are primarily interested in coarsening, we choose the first method. Due to the irregular nature of the dendrite structure, we measure the spacings for many dendrites grown under different supercoolings, normalize all lengths by the tip radius, and analyze the results statistically. The supercoolings vary from 0.23 to 0.78 K, which give tip radii ranging from 19 to 72 μm.

Figure 2 schematically illustrates the measurements performed in the present study. For the spacing, special care must be taken to perform the measurements in a consistent and reproducible manner. We propose a procedure that is based on first determining the contour of the primary stem of the dendrite, and then projecting every valley point between sidebranches onto this stem contour line. The sidebranch spacing is then defined as the distance between two neighboring points on the stem contour (Fig. 2).

The primary stem contour in the initial sidebranching regime is simply a best fit of all sidebranch valley coordinates. In the region far from the tip, we define the primary stem to be the envelope of the *inactive* valleys only, where a valley is judged to be inactive when it is deeper than its two or three neighboring valleys (Fig. 2). According to this definition, the area under the stem contour is almost 100% solid.

In addition to the sidebranch spacing, we measured a number of other geometrical parameters that are used in the following analysis. They include the envelope of the active or surviving sidebranch tips, X_{env}, the contour length, U, and the projection area, F, all of which are illustrated in Fig. 2. A detailed discussion of these three parameters can be found in Ref. [14]. It should be noted, however, that we repeated the measurements of Ref. [14] using higher resolution images. All new measurements agree with the ones of Ref. [14] to within our stated measurement accuracy (see below), except for the contour length, U. The higher resolution allows

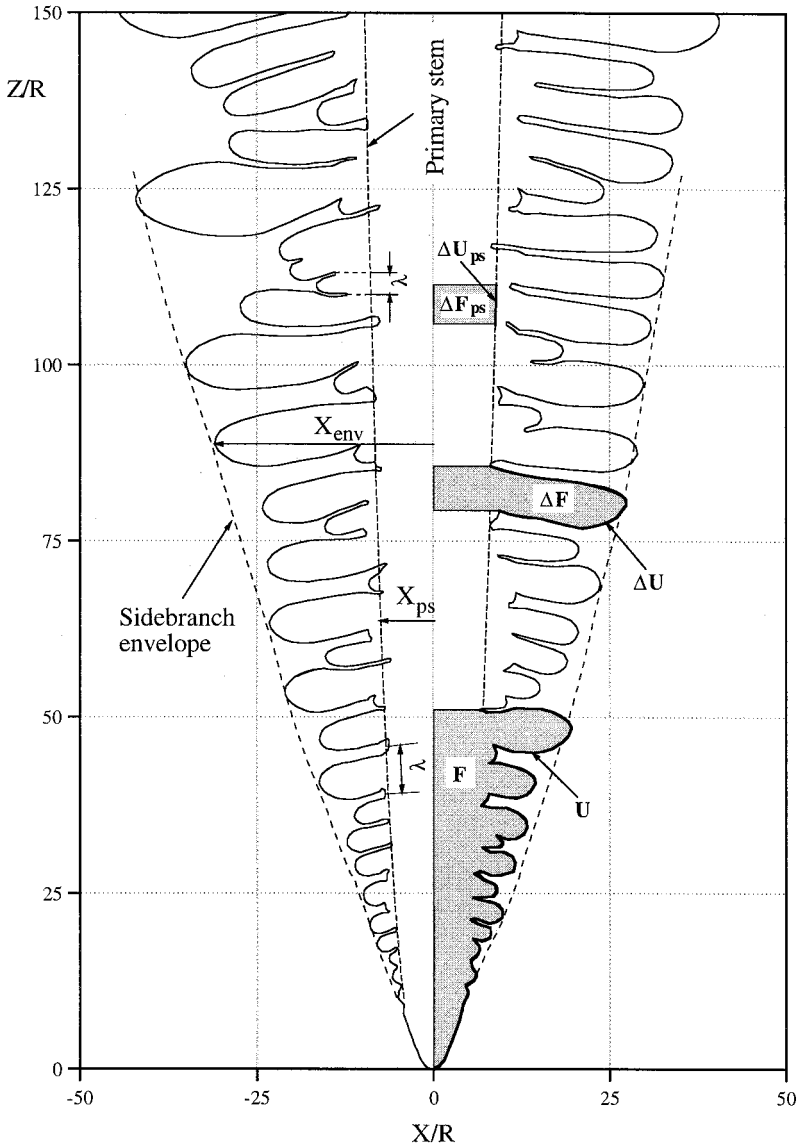

Fig. 2. Schematic illustration of the measurements performed in the present investigation.

for a better identification of the sidebranch valleys, which resulted in a significant change in the measured contour length.

3. RESULTS AND DISCUSSION

Figures 3, 4 and 5 show the results of the present sidebranch spacing, projection area and contour length measurements, respectively, normalized by the tip radius, in log–log plots. The measurements clearly show that: (i) the dendrites are self-similar and can be scaled with the tip radius (which varies by about a factor of four in the present measurements; see above) and (ii) there exist two different regimes that are divided at about $Z/R = 30$. The two regimes correspond to the initial linear and the subsequent non-linear sidebranching regimes mentioned in Section 1 and are analyzed in separate sub-sections below.

3.1. Initial linear sidebranching regime

The initial sidebranching regime of a dendrite is characterized by the growth of the first few branches newly formed near the dendrite tip. The measured sidebranch spacings, projection area and contour length in this regime all fall into a narrow band in Figs 3–5, respectively, demonstrating that the initial sidebranch formation is a well-defined instability that can be scaled with the tip radius. A power law fit of the measured spacing data for $Z/R<30$ gives the variation of the average spacing $\langle\lambda\rangle$ with Z as

$$\langle\lambda\rangle/R = (1.69 \pm 0.16)(Z/R)^{0.198 \pm 0.015}. \qquad (3)$$

Similar fits of the data for the projection area F for

$Z/R<30$ and the data for the contour length U for $Z/R<20$ yield the following scaling relations:

$$F/R^2 = (0.847 \pm 0.04)(Z/R)^{1.598 \pm 0.03} \quad (4)$$

$$U/R = (0.887 \pm 0.03)(Z/R)^{1.116 \pm 0.03}. \quad (5)$$

The error bands for the pre-factors and the exponents were obtained by considering the uncertainties in both the present measurements and the tip radius measurements [15]. It should be mentioned that the experimental correlations for F and U provided in Ref. [14] are different because in our previous study we only correlated the data for $Z/R \gg 1$.

Using the spacing measurement result [equation (3)], we first tested Langer's model [equation (1)] and Brener and Temkin's model [equation (2)], and found that both theories show a discrepancy with the measurement that cannot be explained by measurement error. Even for Brener and Temkin's model, which is based on the more realistic nonaxisymmetric needle crystal shape and has previously shown good agreement with experimental measurements of the sidebranch amplitude [9], there still is a nearly 30% deviation from the present SCN data for the sidebranch spacings (see Fig. 3). In order to overcome this shortcoming of the previous models in the sidebranch spacing prediction, we develop in the following a simple model of the initial sidebranch spacing development that is based on a Mullins–Sekerka instability analysis performed on the needle crystal surface. Although the analysis of Brener and Temkin is much more sophisticated and rigorous, we believe that some of the simplifications they made in their analysis lead to the above noted discrepancy with the measurements.

For a planar solidification front growing into a pure supercooled melt with a steady velocity V_0, Mullins–Sekerka's linear stability analysis [1] shows that the evolution of a sinusoidal perturbation of infinitesimal amplitude δ and wavenumber ω on the interface is determined by the following dispersion relation:

$$\frac{\dot{\delta}}{\delta} = -\frac{\omega}{L}[k_s G_s + k_l G_l + (k_s + k_l)\Gamma\omega^2] \quad (6)$$

where $\dot{\delta} \equiv \mathrm{d}\delta/\mathrm{d}t$, G_l and G_s are the thermal gradients at the unperturbed flat interface ($\delta = 0$) in the liquid and solid, respectively, k_s and k_l are the solid and liquid thermal conductivities, respectively, and $\Gamma = T_m\gamma_{sl}/L$ is the Gibbs–Thomson coefficient in which γ_{sl} is the surface free energy, T_m is the melting temperature, and L is the latent heat. The condition for marginal stability of the interface (i.e. $\dot{\delta}/\delta = 0$) gives the critical wavenumber as

$$\omega_c^2 = -\frac{1}{\Gamma}\frac{k_s G_s + k_l G_l}{k_s + k_l} = -\frac{1}{\Gamma}\bar{G} \quad (7)$$

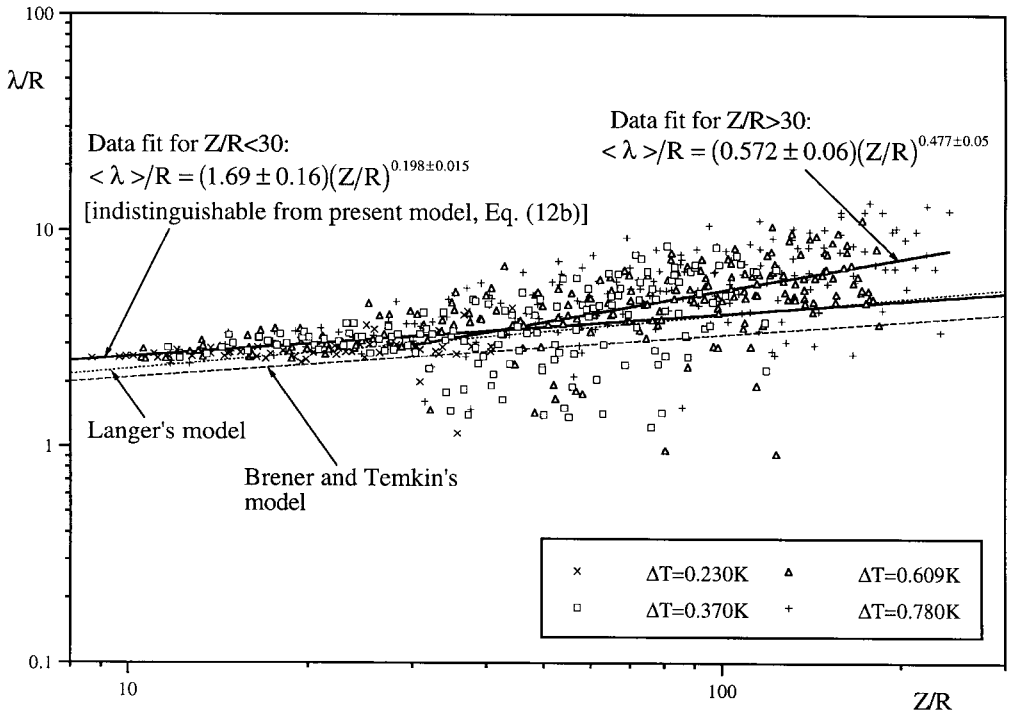

Fig. 3. Measured normalized secondary arm spacings (symbols), λ/R, as a function of the normalized distance, Z/R, from the primary tip; the two solid lines represent a best fit of the data for $Z/R<30$ and $Z/R > 30$, respectively; the interrupted lines are model results for the initial linear sidebranching regime (with $\sigma = 0.02$).

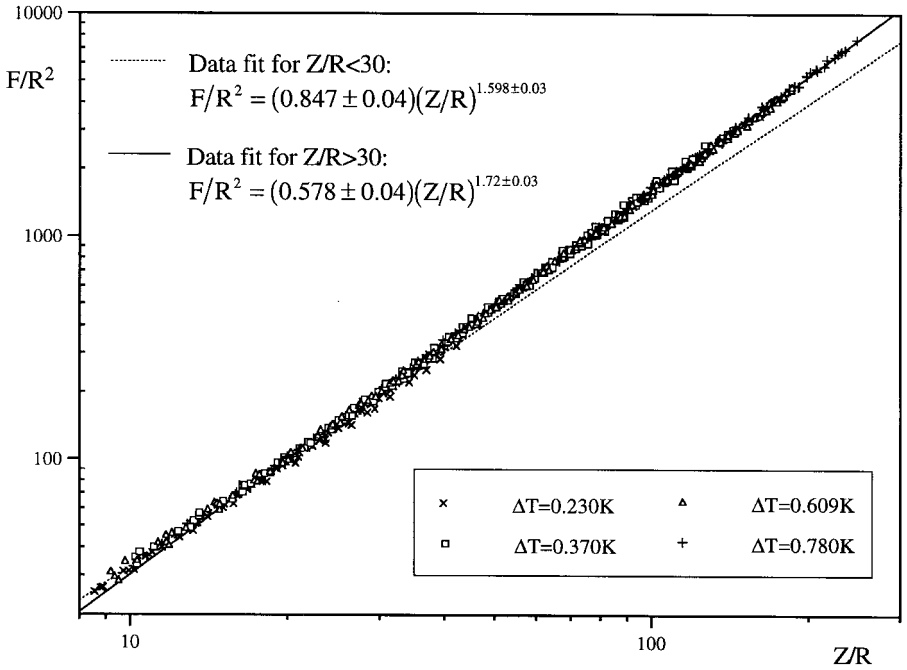

Fig. 4. Normalized projection area, F/R^2, vs normalized distance from the tip, Z/R; the two lines represent a best fit of the data for $Z/R<30$ and $Z/R > 30$, respectively.

where

$$\bar{G} = \frac{k_s G_s + k_l G_l}{k_s + k_l}$$

is the conductivity-weighted average thermal gradient at the flat crystal–melt interface. Equation (7) shows that the solidification front of a pure substance is unstable only if $\bar{G}$ is negative. In the present case of free growth into a supercooled melt, the thermal gradient within the solid, G_s, is zero, and the thermal conductivities of the solid and liquid can be taken to be approximately equal, such that $\bar{G} = \frac{1}{2} G_l$. From an energy balance (or Stefan condition) at the interface, the unperturbed thermal

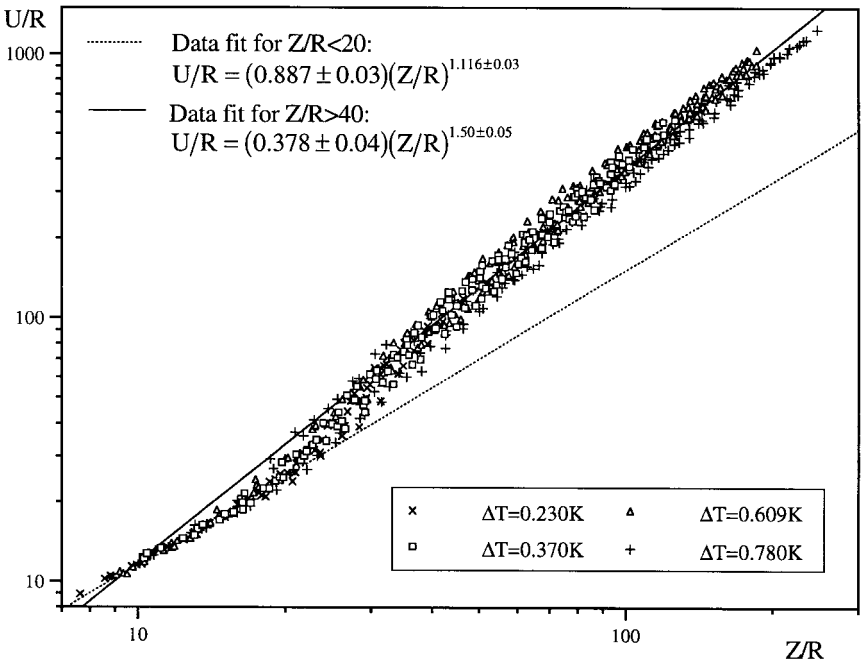

Fig. 5. Normalized contour length, U/R, vs normalized distance from the tip, Z/R; the two lines represent a best fit of the data for $Z/R<20$ and $Z/R > 40$, respectively.

gradient on the liquid side is found to be $G_l = -V_0 L/\alpha_l c_p$, where α_l and c_p are the thermal diffusivity and specific heat, respectively, of the liquid. Then equation (7) gives the critical wavelength, λ_c, as

$$\lambda_c = \frac{2\pi}{\omega_c} = 2\pi\left(\frac{2\alpha_l d_0}{V_0}\right)^{1/2} = 2\pi\sqrt{d_0 l_{th}} \qquad (8)$$

which is simply the root-mean product of the two relevant physical length scales. Here $l_{th} = 2\alpha_l/V_0$ is the thermal length and d_0 is the capillary length defined by $d_0 = \gamma_{sl} c_p T_m/L^2$. The maximum instability wavelength, λ_m, which has the highest rate of growth of the perturbations ($\dot{\delta}/\delta = \text{maximum}$) and establishes the length scale that is likely to be observed experimentally, can be easily found to be

$$\lambda_m = \frac{2\pi}{\omega_m} = 2\pi\sqrt{3 d_0 l_{th}} = \sqrt{3}\lambda_c. \qquad (9)$$

The Mullins–Sekerka instability is directly related to the local thermal gradient at the interface (or the interface velocity), which can be determined by a linear approximation of the thermal field near the interface. Therefore, a curved interface can be expected, within the present linear approximation, to have the same critical and maximum instability wavelengths as derived above for a planar interface. This localizability of the Mullins–Sekerka instability allows the use of the same stability analysis in the study of dendritic sidebranching.

Let us now consider a steady-state needle crystal, $Z/R = \xi_0(X/R, Y/R)$, growing with a constant tip velocity, V_t, and tip radius, R, into a supercooled melt of infinite extent. We treat the interface of the needle crystal in the vicinity of an arbitrary point X/R, Y/R, $Z/R = \xi_0(X/R, Y/R)$ as a piece of a tangential plane moving with the normal velocity V_n, which is equivalent to V_0 in the previous linear stability analysis. The characteristic wavelengths (λ_c and λ_m) of a local instability on the needle crystal surface hence depend only on the local normal interfacial velocity, V_n, according to equations (8) and (9). Obviously, different needle crystal shapes will result in different relationships between V_t and V_n. For an axisymmetric needle crystal (paraboloid), $Z = (X^2 + Y^2)/(2R)$, we have

$$V_n = V_t(1 + 2Z/R)^{-1/2}. \qquad (10a)$$

For a nonaxisymmetric three-dimensional needle crystal, only the four ridges of the crystal, where the sidebranching occurs, need to be considered. According to Brener [8], the contour of the ridges is given by $X/R = (\sigma/\sigma_2)^{1/5}(\frac{5}{3}Z/R)^{3/5}$. Omitting the factor $(\sigma/\sigma_2)^{1/5}$, which is very close to unity, yields the following expression for V_n along the ridges

$$V_n = V_t[1 + (\tfrac{5}{3}Z/R)^{4/5}]^{-1/2}. \qquad (10b)$$

Substituting equations (10a) and (10b) into equations (8) and (9), and using the usual selection criterion for the dendrite tip operating state $\sigma = 2\alpha_l d_0/V_t R^2$, the variations of the local critical wavelength λ_c and the local maximum instability wavelength λ_m with distance away from the primary tip, Z, for the two different needle crystal shapes are given by

axisymmetric needle crystal:

$$\lambda_c/R = 2\pi\sqrt{\sigma}(1 + 2Z/R)^{1/4} \approx 1.06(Z/R)^{1/4} \qquad (11a)$$

$$\lambda_m/R = 2\pi\sqrt{3\sigma}(1 + 2Z/R)^{1/4} \approx 1.84(Z/R)^{1/4} \qquad (11b)$$

nonaxisymmetric needle crystal:

$$\lambda_c/R = 2\pi\sqrt{\sigma}[1 + (\tfrac{5}{3}Z/R)^{4/5}]^{1/4} \approx 0.99(Z/R)^{1/5} \qquad (12a)$$

$$\lambda_m/R = 2\pi\sqrt{3\sigma}[1 + (\tfrac{5}{3}Z/R)^{4/5}]^{1/4} \approx 1.72(Z/R)^{1/5}. \qquad (12b)$$

The approximate expressions are curve fits for $8 < Z/R < 30$ and an experimental value of $\sigma = 0.02$ for SCN [6]. The above analysis shows that the direct incorporation of the Mullins–Sekerka linear stability analysis for a planar interface into dendrite growth models allows one to determine the sidebranch spacing for a given needle crystal shape in a very simple way. This is the most appealing feature of the present model.

Equations (11) and (12) are identical in form to equation (1) from Langer's model [4] and equation (2) from Brener and Temkin's model [7], respectively, except for the value of the pre-factor. The agreement with those more sophisticated models implies that the present model, despite its simplicity, is essentially correct. The pre-factors in both of the previous models are between the pre-factors for the critical, λ_c, and maximum, λ_m, instability wavelengths in the present model, but somewhat closer to λ_c.

Since the present model, using λ_m, predicts a larger sidebranch spacing for both crystal shapes than the previous models, the above noted discrepancy in the sidebranch spacing between the previous models and experiments can be reduced. For example, at a distance of $Z/R = 7$–9, where the first clear sidebranches can be observed in Huang and Glicksman's earth-based experiments for SCN [6], the dimensionless spacings, λ_m/R, predicted by the present model [equations (11b) and (12b)] are 3.1 and 2.7 for the two crystal shapes. Both of these values are in much better agreement with the experimental value of 3.0 than the value of $\lambda/R \approx 2.0$–2.1 predicted by Langer's and Brener and Temkin's models. Hürlimann *et al.* [12] measured a normalized initial sidebranch spacing near the tip of 3.2 ± 0.4 (and a σ of 0.02) in their experiments with xenon dendrites, again indicating better agreement with the present model than with Langer's and

Brener and Temkin's predictions. These preliminary comparisons with experiments for two different substances suggest that the maximum instability wavelength is indeed selected as the initial sidebranch spacing. However, some uncertainties remain due to the possible influence of convection in the earth-based experiments of Refs [6, 12].

The present arm spacing measurements, being made on dendrites grown in a convection-free environment, allow for a more conclusive comparison with the model over the entire linear sidebranching regime, which is shown in Fig. 3. Both the exponent of 0.198 ± 0.015 and the pre-factor of 1.69 ± 0.16 in the experimental correlation, equation (3), are in excellent agreement with the present model for the maximum instability wavelength of the nonaxisymmetric needle crystal [equation (12b)]. This good agreement not only validates our simple model but also confirms that: (i) the maximum, and not the critical, instability wavelength determines the observed initial sidebranch spacing and (ii) the nonaxisymmetric needle crystal of Brener [8] gives a more realistic dendrite shape. Furthermore, since the present model relies directly on the Mullins–Sekerka stability theory, the present comparison can be regarded as an experimental validation of this important theory.

While the selection mechanism of the initial sidebranch spacings is well clarified by the present spacing measurement and model, the projection area measurement allows us to demonstrate another important growth mechanism of dendritic crystals. The nonaxisymmetric needle crystal model of Brener [8] gives the following analytical result for the projection area, F, in the sidebranch plane

$$F/R^2 \approx 0.85(Z/R)^{1.6}. \tag{13}$$

The present correlation of the $F(Z)$ measurements [equation (4)] shows the same scaling exponent of 1.6 and the same pre-factor of 0.85 to within the measurement uncertainty. The fact that real dendrites with sidebranches and a needle crystal (without sidebranches) have the same projection area indicates that the theoretical steady-state solution is preserved in some geometrical parameters (the projection area here) of the actual dendritic patterns. Similar results have been reported by Couder *et al.* [16] for two-dimensional dendritic growth, anisotropic viscous fingering, and anisotropic diffusion-limited aggregation. While the projection area is exactly preserved in the initial linear regime, we can see from Fig. 4 a small deviation of $F(Z)$ from that of the needle crystal in the non-linear regime. This deviation may be attributed to coarsening, which is discussed in the next section.

3.2. Non-linear regime

As the sidebranches evolve into a non-linear regime far down from the tip, a coarsening phenomenon occurs during which some sidebranches continue to grow as others are squeezed out, resulting in a very irregular sidebranch structure. It is presently not clear whether this coarsening process can be described by available theories. The classical description of coarsening by Lifshitz and Slyozov [17] and Wagner [18] (LSW) assumes an isothermal system, a vanishingly small solid volume fraction, and spherical particles. Then, in the limit of infinite time, the steady-state particle size distribution scaled by the mean particle size was found to be time invariant, and the mean particle radius, $\bar{\rho}$, was shown to increase with the cube root of time, t (i.e. $\bar{\rho} \sim t^{1/3}$). None of the above assumptions are satisfied for the present dendrite sidebranching system. More recent theories have shown that the coarsening rate exponent of 1/3 remains unaltered for finite solid volume fractions and certain non-spherical particle geometries, but the constant of proportionality in the temporal power law and the particle size distribution change. The possible effect of non-isothermality and the resulting net solidification, as present in free dendritic growth, has not been investigated theoretically. Hence, the purpose of this section is simply to define and measure meaningful geometrical parameters of sidebranching dendrites in the non-linear coarsening regime, and to assess the need to develop new theories of coarsening of the sidebranch structure in free dendritic growth.

As can be seen from Fig. 3, the experimental data for the sidebranch spacing become, after $Z/R = 30$, very dispersed. The fluctuations in the measured spacings reflect the dynamic adjustment process of the arm spacing through competitive growth and capillary-driven coarsening. In spite of the fluctuations, we can still observe an increasing trend in the spacing with Z in the experimental data. A least-squares fit of all data for $Z/R > 30$ by a power law yields

$$\begin{aligned}\langle\lambda\rangle/R &= (0.572 \pm 0.06)(Z/R)^{0.477 \pm 0.05} \\ &= (0.572 \pm 0.06)(V_t t/R)^{0.477 \pm 0.05}.\end{aligned} \tag{14}$$

The second equality simply states that $Z = V_t t$ in steady dendritic growth. The exponent of 0.477 is much different from the classical coarsening exponent of 1/3 (i.e. $\lambda \sim t^{1/3}$). Likely, the disagreement in the exponent is due to the fact that the arm spacing is not an appropriate geometrical parameter for comparison with available coarsening theories.

Another geometrical parameter that has been used to characterize coarsening in the non-linear regime is the projection area per unit contour length in the sidebranch plane, normalized by the tip radius, i.e. $F/(UR)$ [12, 14]. By including both growing and shrinking sidebranches, this dimensionless parameter can be associated with a normalized mean branch radius [12]. The present measurement

of the projection area F for $Z/R > 30$ is well correlated by (Fig. 4)

$$F/R^2 = (0.578 \pm 0.04)(Z/R)^{1.72 \pm 0.03} \quad (15)$$

which is in close agreement with our previous result [14]. Similarly, our measurement of the contour length U for $Z/R > 40$ is well correlated by (Fig. 5)

$$U/R = (0.378 \pm 0.04)(Z/R)^{1.50 \pm 0.05}. \quad (16)$$

The exponent of 1.5 in equation (16) should be contrasted with an exponent of 1.7 measured previously [14]. Differences between equation (16) and our previous result [14] are apparent only at large Z/R, and we believe that the present measurement is more accurate because it is based on higher resolution images. Combining equations (15) and (16) yields

$$\frac{F}{UR} = 1.529(Z/R)^{0.22}. \quad (17)$$

As opposed to the previous studies [12, 14], the present result for $F/(UR)$ is not a constant in the non-linear regime, but is a function of Z/R. As with the sidebranch spacing, equation (14), the exponent of 0.22 is not close to the classical coarsening exponent of 1/3, indicating that $F/(UR)$ is not an appropriate parameter for comparison with available coarsening theories.

As discussed by Marsh and Glicksman [19], a sidebranching dendrite has many (positive and negative) curvatures and it is presently not clear how the coarsening of a dendrite can be described quantitatively. In the following we explore this issue in more detail by proposing two new geometrical parameters, both being characteristic branch radii, that are intended to better characterize the mean curvature and perhaps allow for a better comparison with coarsening theories.

3.2.1. Branch radius at the root ρ_r. The reciprocal of the radius of the branches deep inside the sidebranch structure near the junction between an arm and the primary stem is likely to be a dominant curvature controlled by isothermal coarsening. Due to the difficulty of measuring such a root radius, ρ_r, directly from the images, we propose to calculate it from the measured arm spacings and an estimate of the local area fraction solid, f_a, in the sidebranch plane of Fig. 2. Since for an array of cylindrical arms the diameter is equal to the spacing times the area fraction of solid, we have that $\rho_r = f_a\lambda/2$, and equation (14) can be converted to

$$\langle\rho_r\rangle/R = 0.286 f_a (Z/R)^{0.477} = 0.286 f_a (V_t t/R)^{0.477}. \quad (18)$$

The local area fraction f_a may be estimated by dividing an axial section of the (solid) area F in Fig. 2 by the (liquid plus solid) area, F_{env}, under the sidebranch envelope for the same section. The sidebranch envelope measurement, $X_{env}/R = 0.668(Z/R)^{0.859}$ taken from Ref. [14] and verified here, allows for the calculation of the projection area of the sidebranch envelope, F_{env}, as

$$F_{env}/R^2 = 0.359(Z/R)^{1.859}. \quad (19)$$

Using equation (15) for the projection area F, the local area fraction is then given by

$$f_a = \mathrm{d}F/\mathrm{d}F_{env} = 1.488(Z/R)^{-0.139}. \quad (20)$$

According to this equation, the local solid area fraction varies from about 0.93 at $Z/R = 30$ to 0.74 at $Z/R = 150$, which appears to be realistic looking at Fig. 1. Substituting equation (20) into equation (18) yields

$$\langle\rho_r\rangle/R = 0.426(Z/R)^{0.338} = 0.426(V_t t/R)^{0.338}. \quad (21)$$

The above result shows a coarsening exponent very close to the general coarsening exponent of 1/3 and suggests that the branch radius at the root ρ_r is a suitable parameter for characterizing coarsening of the sidebranches in the non-linear regime. In the following, a preliminary comparison is made with other theories regarding the value of the coarsening rate constant (i.e. the pre-factor) and the radius distribution.

Classical LSW theory describes the coarsening behavior of spherical particles in the limit of zero volume fraction solid as

$$\bar{\rho}^3(t) - \bar{\rho}_0^3 = \frac{8}{9}\alpha_l d_0 t = K_{LSW} t \quad (22)$$

where $\bar{\rho}_0$ is the initial mean particle radius, and $K_{LSW} = \frac{8}{9}\alpha_l d_0$ is the coarsening rate constant. At long times, equation (22) attains the asymptotic form $\bar{\rho}(t) \propto t^{1/3}$. In order to make a quantitative comparison with the measured coarsening rate constant, we rewrite our measurement result, equation (21), as

$$\langle\rho_r\rangle^3 = 0.0773(R^2 V_t)t = 0.0773\left(\frac{2\alpha_l d_0}{\sigma}\right)t = 7.73\alpha_l d_0 t. \quad (23)$$

Not surprisingly, the above result shows a much larger coarsening rate constant than LSW theory [equation (22)]. More realistic models that take into account the effect of finite volume fractions of solid have been developed [20–22]. For example, at a volume fraction of 0.8, a reasonable value in the root region of the branches, Marsh and Glicksman's model [21] predicts a coarsening rate constant of $8.93\alpha_l d_0$, which is quite close to the present measurement value. Although this comparison is preliminary, it does show that the sidebranch root radius is likely to be a meaningful parameter in describing coarsening during dendritic growth.

Converting the measured spacings λ into the root branch radius ρ_r one by one according to the for-

mula $\rho_r = f_a\lambda/2$, we also examined the size distribution of ρ_r. The result, which is given in terms of ρ_r renormalized by the average radius $\langle\rho_r\rangle$, is presented in Fig. 6. For comparison we also plot the theoretical distribution functions obtained by LSW [17, 18], Marsh and Glicksman [21] for three-dimensional coarsening at a volume fraction $f_v = 0.6$, and Ardell [23] for two-dimensional coarsening at $f_v = 0.3$.

It can be seen from Fig. 6 that our experimental result shows a much broader distribution with a much lower peak than the LSW prediction. However, comparing with the models that take into account the effect of finite volume fraction, the agreement becomes better except that the measured distribution is more symmetrical and the distribution peak is closer to 1 (see Fig. 6). We can also notice that the experimentally measured distribution seems to be in better agreement with the two-dimensional model than the three-dimensional model. Considering that the sidebranches grow along a row on the four ridges of the dendrite and that the sidebranches on different ridges may communicate only weakly, the coarsening at the root of the sidebranches may indeed be more like a two-dimensional process rather than a three-dimensional process. Since there are, to the authors' knowledge, no two-dimensional coarsening models available for volume fractions beyond $f_v = 0.5$, we cannot make a more direct comparison with two-dimensional coarsening theories.

3.2.2. Mean sidebranch radius ρ_m. As indicated in the previous section, the branch radius ρ_r only reflects the coarsening phenomenon near the branch root. We therefore propose another parameter, a mean sidebranch radius ρ_m, to characterize the overall coarsening process of a free dendrite branch.

The mean sidebranch radius ρ_m is not derived from the branch spacing measurements, but from measurements of the primary stem shape, its projection area F_{ps} and its contour length U_{ps}, and the projection area F and the contour length U of a dendrite (Fig. 2). The idea is based on the fact that the quantity $(\Delta F - \Delta F_{ps})/(\Delta U - \Delta U_{ps})$ is an area-averaged radius of a sidebranch if we approximate a branch as a cylindrical rod. The quantities ΔF, ΔF_{ps}, ΔU and ΔU_{ps} are shown in Fig. 2 to illustrate this concept. Since we have correlated all measurements as continuous functions of Z, we can use the following differential definition for the mean sidebranch radius ρ_m:

$$\rho_m = (dF - dF_{ps})/(dU - dU_{ps}). \tag{24}$$

The present measurements of the primary stem shape X_{ps}/R are well correlated by (not plotted)

$$X_{ps}/R = (2.26 \pm 0.14)(Z/R)^{0.316 \pm 0.02} \quad \text{for } Z/R > 30. \tag{25}$$

From equation (25), we can determine F_{ps} and U_{ps} of the primary stem as

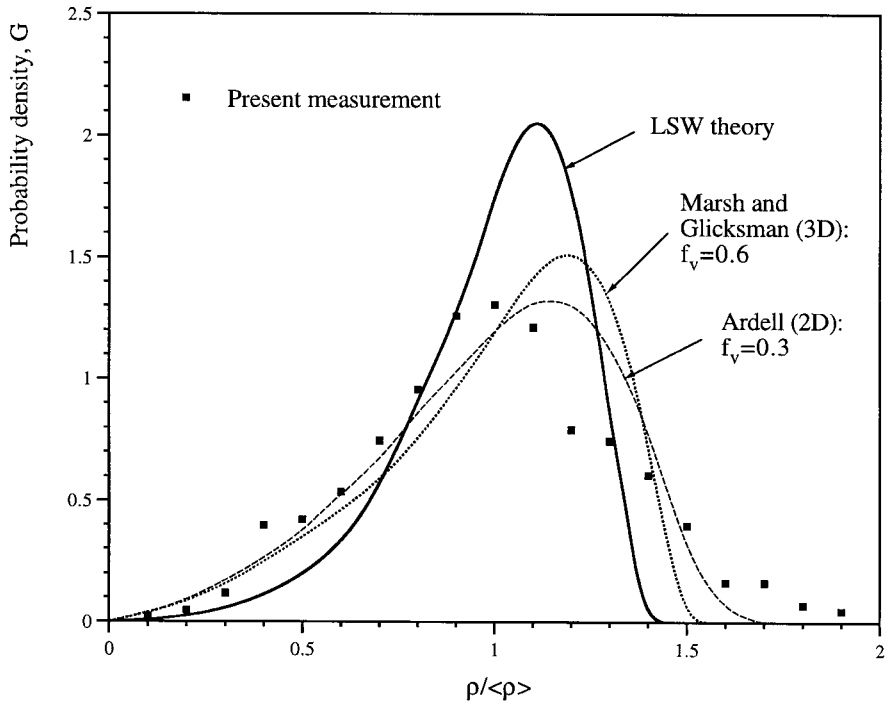

Fig. 6. Comparison of size distributions derived from isothermal coarsening theories with the present measurements of the distribution of the sidebranch radii at the root. The area under the distribution is normalized to unity.

$$F_{ps}/R^2 = 1.72(Z/R)^{1.32} \text{ for } Z/R > 30 \quad (26a)$$

$$U_{ps}/R \approx 1.02(Z/R)^{0.996} \text{ for } Z/R > 30. \quad (26b)$$

According to the definition of ρ_m [equation (24)], we then obtain

$$\rho_m = \frac{dF - dF_{ps}}{dU - dU_{ps}} = \left[\frac{0.994(Z/R)^{0.72} - 2.27(Z/R)^{0.32}}{0.567(Z/R)^{0.50} - 1.016(Z/R)^{-0.004}}\right]R. \quad (27)$$

For $40<Z/R<200$, the above equation can be well approximated by a power law

$$\rho_m/R \approx 0.801(Z/R)^{0.341} = 0.801(V_t t/R)^{0.341}. \quad (28)$$

Again, the exponent of 0.341 is in good agreement with the classical coarsening exponent of 1/3. Using a slightly less accurate cubic root approximation of equation (28), given by $\rho_m/R \approx 0.830(V_t t/R)^{1/3}$, we obtain

$$\rho_m^3 = 0.572(R^2 V_t)t = 0.572(2\alpha_l d_0/\sigma)t = 57.2\alpha_l d_0 t. \quad (29)$$

The above equation shows a much larger coarsening rate constant than the one we obtained for the root radius, equation (23). Such a large rate constant cannot be explained using available theories for isothermal two-phase coarsening at a finite solid fraction, e.g. Refs [19–22]. A reason for the discrepancy could be that the sidebranches on a free dendrite have close neighbors only in the Z direction, while they are surrounded by supercooled melt in the circumferential direction and in the tip region. In particular in the tip region of the active (or growing) sidebranches, coarsening is controlled by heat transfer between the interface and the supercooled melt (net solidification) and competitive growth. Hence, the overall sidebranch coarsening process in free dendritic growth is driven by the combined effects of net solidification and interfacial energy reduction. Interestingly, the measured coarsening exponent shows excellent agreement with theories of purely capillary-driven coarsening. Only a more complete analysis of non-isothermal coarsening, with net solidification, can clarify this matter.

4. CONCLUSIONS

A detailed measurement of the sidebranch structure of freely growing succinonitrile (SCN) dendrites is performed using images from the microgravity experiment of Glicksman and coworkers. The measurements reveal two different regimes in the sidebranching evolution: an initial linear regime and a subsequent non-linear coarsening regime. A simple model, based on the Mullins–Sekerka linear stability theory, is developed to describe the initial sidebranching behavior and is found to be in excellent agreement with the experimentally measured arm spacings. It is found that the initial sidebranch spacings are selected by the maximum instability wavelength. In addition, the result of the projection area measurement suggests preservation of the steady-state solution (needle crystal) in the dendrite volume during three-dimensional dendritic growth. In the non-linear regime, the measured arm spacings demonstrate a coarsening behavior quite different from classical laws for purely capillary-driven isothermal coarsening. On the other hand, the equivalent radius at the sidebranch root, obtained from the measured arm spacings, appears to compare well with previous isothermal coarsening theories for finite volume fractions of solid. Another parameter, the mean sidebranch radius, is developed to characterize the coarsening process of a whole sidebranch in free dendritic growth. It is obtained from measurements of the projection area, the contour length and the primary stem shape. While its coarsening behavior follows the classical cube root of time law, the large coarsening rate constant suggests that new theories of non-isothermal coarsening need to be developed to explain the measurements completely.

Acknowledgements—This work was supported by NASA under contract NCC8-94. The authors are indebted to M. E. Glicksman of RPI and NASA for making the IDGE images available to us.

REFERENCES

1. Mullins, W. W. and Sekerka, R. F., *J. appl. Phys.*, 1964, **35**, 444.
2. Langer, J. S. and Müller-Krumbhaar, H., *Acta metall.*, 1978, **26**, 1681.
3. Pieters, R. and Langer, J. S., *Phys. Rev. Lett.*, 1986, **56**, 1948.
4. Langer, J. S., *Phys. Rev.*, 1987, **A36**, 3350.
5. Barber, M. N., Barbieri, A. and Langer, J. S., *Phys. Rev.*, 1987, **A36**, 3340.
6. Huang, S. C. and Glicksman, M. E., *Acta metall.*, 1981, **29**, 701.
7. Brener, E. and Temkin, D., *Phys. Rev.*, 1995, **E51**, 351.
8. Brener, E., *Phys. Rev. Lett.*, 1993, **71**, 3653.
9. Bisang, U. and Bilgram, J. H., *Phys. Rev. Lett.*, 1995, **75**, 3898.
10. Bisang, U. and Bilgram, J. H., *Phys. Rev.*, 1996, **E54**, 5309.
11. LaCombe, J. C., Koss, M. B., Fradkov, V. E. and Glicksman, M. E., *Phys. Rev.*, 1995, **E52**, 2778.
12. Hürlimann, E., Trittibach, R., Bisang, U. and Bilgram, J. H., *Phys. Rev.*, 1992, **A46**, 6579.
13. Dougherty, A. and Chen, R., *Phys. Rev.*, 1992, **A46**, R4508.
14. Li, Q. and Beckermann, C., *Phys. Rev.*, 1998, **E57**, 3176.
15. Glicksman, M. E., Koss, M. B. and Winsa, E. A., *Phys. Rev. Lett.*, 1993, **73**, 573.
16. Couder, Y., Argoul, F., Arneodo, A., Maurer, J. and Rabaud, M., *Phys. Rev.*, 1990, **A42**, 3499.
17. Lifshitz, I. and Slyozov, V., *J. Phys. Chem. Solids*, 1961, **19**, 35.

18. Wagner, C., *Z. Elektrochem.*, 1961, **65**, 581.
19. Marsh, S. P. and Glicksman, M., *Metall. Trans. A*, 1996, **27A**, 557.
20. Voorhees, P. and Glicksman, M., *Acta metall.*, 1984, **32**, 2013.
21. Marsh, S. P. and Glicksman, M., *Acta mater.*, 1996, **44**, 3761.
22. Akaiwa, N. and Voorhees, P., *Phys. Rev.*, 1994, **E49**, 3860.
23. Ardell, A. J., *Phys. Rev.*, 1990, **B41**, 2554.